analytical chemistry

pubs.acs.org/ac Article

Integrating Near-Infrared Visual Fluorescence with a Photoelectrochemical Sensing System for Dual Readout Detection of Biomolecules

Qingzhi Han, Xuan Zhao, Na Na, and Jin Ouyang*

Cite This: *Anal. Chem.* 2021, 93, 3486−3492 Read Online

ACCESS | Metrics & More | Article Recommendations | Supporting Information

ABSTRACT: Compared with traditional visible light-driven fluorescence visualization (FV), near-infrared (NIR)-induced FV is an interesting and promising method, while photoelectrochemical (PEC) immunoassay sensing possesses the advantages of high sensitivity, low cost, and simple instrumentation. We combined PEC sensing with NIR-induced FV together and developed a dual readout sensing platform. In this protocol, based on the antibody−analyte (i.e., antigen, DNA, and RNA) reaction and the sandwich-type structure, $CuInS_2$ microflowers as the matrix provided the original background photocurrent; chlorin e6 (Ce6) was conjugated to antibody-modified upconversion nanoparticles and formed a signal label for the PEC sensing and naked-eye readout. Different from traditional PEC immunosensors, under NIR illumination, the developed dual mode sensing platform could achieve quick qualitative analysis and quantitative analysis. Preliminary application performance of the proposed biosensor in prostate-specific antigen analysis is acceptable, indicating its promising potential in clinical/biological studies.

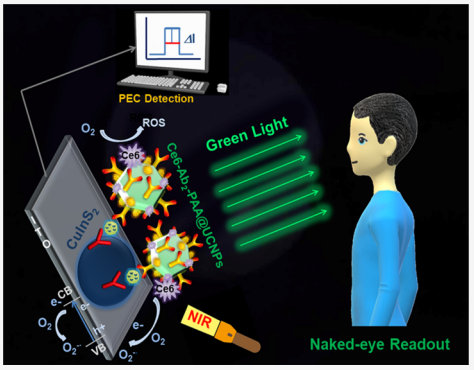

INTRODUCTION

The fluorescence visualization (FV) technique is a potentially powerful and rapidly growing approach in analytical testing (environmentally or biologically).[1−3] Under specific light irradiation, the recognition site could specifically conjugate with its corresponding analyte and emit visible light, which could be observed via the naked eye.[4] Application of FV in monitor targets is a convenient and simple technique considering the near-infrared FV (NIR-FV)-induced naked-eye readout.[5] Photoelectrochemical (PEC) bioanalysis as a sensitive, low-cost, and promising strategy, contributed by the photoactive species, possesses a separated source for excitation (light) and detection (photocurrent).[6−8] In a typical PEC detection process, light is used to excite the photoactive species (e.g., semiconductors), while the obtained electrical signal is transduced as the output signal. Because PEC detection has separated forms of excitation and detection, its background signals are reduced. Integrating NIR-FV with the PEC technique together is a logical and practical design. Introducing the naked-eye readout into the PEC detection system can make the qualitative process easier than a single PEC method. In addition, the dual mode strategy would benefit large batch detection because the naked-eye readout mode can exclude some samples that contain little targets (within the normal threshold). Moreover, the PEC method and naked-eye readout as two different kinds of mode detection techniques could work as references for each other to improve the accuracy of results.

For PEC bioanalysis, various materials have been used, including n-type semiconductors (e.g., TiO_2, ZnO, CdS, WO_3, etc.) and p-type semiconductors (e.g., BiOI, PbS, $CuInS_2$, NiO, etc.), and they have opposite characteristics.[9−11] p-Type semiconductors are the inverse of n-type semiconductors, which have holes as the major carriers, whereas n-type semiconductors have electrons as their major conductivity carriers.[12−14] Because electrons are the major carriers for n-type semiconductors, the reductive agents (e.g., dopamine, ascorbic acid, etc.)[15] would compete with electron donors and be absorbed on the surface of the sensing electrode, which would result in inaccurate signals; however, p-type semiconductors would overcome the drawbacks of n-type semiconductors (photoanode)[14] because of its hole conduction characteristics. Hence, for the construction of a PEC immunosensor, the p-type semiconductor is more suitable. $CuInS_2$[15−18] as a narrow band-gap (∼1.5 eV) p-type semiconductor has high light usage efficiency. Under NIR illumination, the photogenerated holes of $CuInS_2$ transfer toward the electrolyte solution (Tris−HCl buffer) and generate a cathodic photocurrent.

Received: November 13, 2020
Accepted: January 28, 2021
Published: February 5, 2021

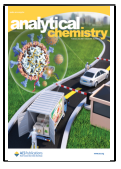

https://dx.doi.org/10.1021/acs.analchem.0c04802
Anal. Chem. 2021, 93, 3486−3492

Lanthanide-doped upconversion nanoparticles (UCNPs) can absorb NIR photons and convert them into shorter wavelength emissions.[19−21] Hexagonal NaYF crystals are a popular host material for green UCNPs when sensitized via Yb^{3+} and activated by Er^{3+}/Tm^{3+} ($NaYF_4$:Yb,Er) and have been widely used in the development of solar cells, lasers, and fluorescence labeling.[22−26] To develop a UCNP-involved biosensor, by means of surface modification to make UCNPs functionalized, water dispersibility and biocompatibility are indispensable. Coating silica onto the surface of UCNPs is a commonly used method to make UCNPs dispersible in water, but in this way, the luminescence intensity would be reduced greatly and is also detrimental to further surface modification.[27] However, replacing the hydrophobic ligands with small hydrophilic ligands (ligand exchange reaction) to make UCNPs water-soluble and be functionalized is better. As a polymer, polyacrylic acid (PAA) usually has an average molecular weight (M_W) of 1800, and we can control the particle growth by decreasing the reactivity of the rare earth ions with fluoride and render nanoparticles small in size and uniform in shape (good crystallization). In addition, the carboxylic groups of PAA also coordinate with the lanthanide ions on the UCNP surface, resulting in a high water solubility of UCNPs. Chlorin e6 (Ce6) is a popular clinical photosensitizer, has high up-sensitizing effects, and usually works as a reactive oxygen species (ROS) generator in photodynamic therapy (PDT) to kill cancer cells.[28,29] Meanwhile, for cathodic PEC analysis, O_2 is the main electron acceptor; the generation of ROS would also consume dissolved O_2 in the electrolyte. Therefore, Ce6 can be an O_2 consumer to assist Ab_2-PAA@UCNPs, reducing the cathodic photocurrent.

In this work, we developed a dual mode sensing platform by combining PEC sensing and the naked-eye readout together, using a prostate-specific antigen (PSA, Ag) as a model analyte, and achieved rapid and sensitive bioanalysis. As depicted in Scheme 1, first, PAA was modified onto the surface of oleic acid (OA)-capped UCNPs via a ligand exchange method (PAA@UCNPs), and then, the PSA signal antibody (Ab_2) and Ce6 were conjugated with PAA@UCNPs in turn to form Ce6-Ab_2-PAA@UCNP conjugates as the PEC/FV labels. After that, $CuInS_2$ micro-flowers (MFs) were modified onto a sheet of ITO glass, and then, the PSA capture antibody (Ab_1) was fixed via a cross-linking medium of chitosan (amino/carboxyl interaction). Next, the non-specificity sites were shielded with BSA solution. After that, PSA (antigen, Ag) was added to specifically bind with Ab_1; after that, the Ce6-Ab_2-PAA@UCNP labels were added. In this design, $CuInS_2$ as a photoactive material was used for the photosensitive matrix (providing a big PEC signal: μA level), and Ce6-Ab_2-PAA@UCNPs played as the signal inhibitor/illuminant body and took part in the PEC detection as well as the naked-eye readout. This novel dual-readout sensing platform enables the fast qualitative naked-eye readout and quantitative PEC analysis. The design idea would pave a new way for the sensitive and rapid detection of various biomolecules.

EXPERIMENTAL SECTION

The details of reagents, instruments, the synthesis of $CuInS_2$ micro-flowers, the synthesis of oleic acid-coated $NaYF_4$:Yb,Er nanoparticles, and the photoelectrochemical and fluorescence measurements are provided in the Supporting Information.

Synthesis of PAA-Coated UCNPs. Water-soluble and PAA-functionalized UCNPs were prepared according to the literature method with minor modifications.[30] The surface modification was realized via a ligand exchange method. PAA was used as a multidentate ligand to replace the hydrophobic ligands on the UCNP surface by mixing 1 mL of ethanol, 1 mL of UCNPs, and 15 μL of PAA. The mixture was dispersed in chloroform (~15 mg/mL) for overnight stirring. The product was then centrifuged at 8000 rpm for 10 min. After washing several times via ethanol and water separately, the obtained material was redispersed in 5 mL of water.

Scheme 1. Preparation of the Ce6-Ab_2-PAA@UCNP Bioconjugates and Manufacturing Process of the $CuInS_2$ Matrix-Based Dual-Readout Sensing Platform

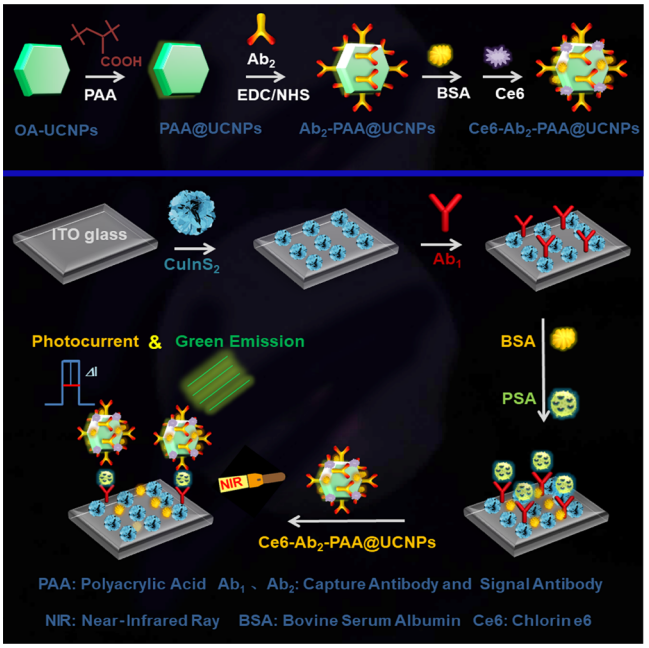

Preparation of Ab_2-PAA@UCNPs. PAA@UCNPs (1 mL) were centrifuged (8500 rpm) and resuspended in 1 mL of MES buffer. EDC (150 μL, 2 mg/mL) and sulfo-NHS (100 μL, 2 mg/mL) were added into the solution, and the reaction lasted for 2 h at 37 °C. Ab_2 solution (1 mL, 10 μg/mL) was added into the solution. The mixture was then incubated for 12 h. Then, the Ab_2-conjugated PAA@UCNPs were centrifuged, washed several times with PBS buffer, and then redispersed in 1 mL of PBS buffer.

Preparation of Ce6-Ab_2-PAA@UCNPs. Preparation of Ce6-Ab_2 conjugates was operated according to a previous report.[29] Ce6 (1 μM) was put in anhydrous DMSO with NHS and EDC dissolved in DMSO for 1.5 h to obtain Ce6-NHS. The coupling reaction between Ce6-NHS and Ab_2-PAA@UCNPs solution (0.5 mg/mL) was carried out at RT for 10 h. To remove excess Ce6, the solution was filtered via an ultrafiltration centrifugal tube (100 K, Millipore, USA) using PBS.

Construction of the NIR-FV and PEC Dual Mode Sensing Platform. Before the modification, the ITO slices (20 × 7 mm^2) were washed with the same method that we previously used.[11] $CuInS_2$ suspension (10 μL, 15 mg/mL) was dropped onto an ITO slice and dried at room temperature. Afterward, the ITO/$CuInS_2$ electrode was annealed at 200 °C in an air atmosphere for 30 min to make $CuInS_2$ combine with the ITO glass tightly. Then, 5 μL of 15 mg/mL chitosan (CS) as a linker was sprayed onto the surface of $CuInS_2$ for Ab_1 (10

https://dx.doi.org/10.1021/acs.analchem.0c04802
Anal. Chem. 2021, 93, 3486−3492

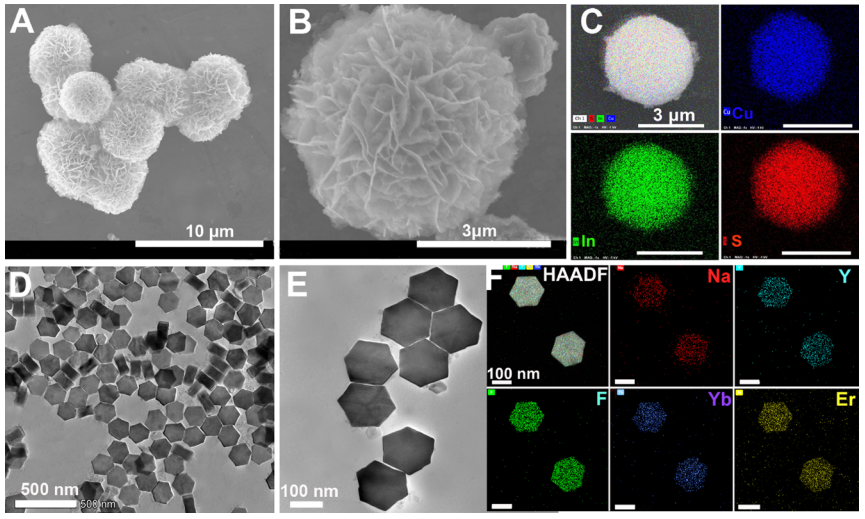

Figure 1. (A, B) SEM images of $CuInS_2$ MFs with different magnifications. (C) SEM-EDS mapping of Cu, In, and S for $CuInS_2$ MFs. (D, E) TEM images of OA-capped $NaYF_4$:Yb,Er (OA-UCNPs). (F) High-angle annular dark-field STEM (HAADF-STEM) image and energy-dispersive X-ray (EDX) elemental mapping of $NaYF_4$:Yb,Er.

μg/mL) modification. Next, various concentrations of PSA were added and then the blocking solution of BSA was added to shield nonspecific binding sites (incubated at room temperature (RT) for 30 min). The final step of the construction process for the dual-readout sensing platform was adding 5 μL of Ce6-Ab_2-PAA@UCNPs (10 μg/mL) to the BSA blocked electrodes and incubating for 40 min at RT. After each step, the surface of the modified electrode was rinsed with PBS buffer thoroughly.

RESULTS AND DISCUSSION

Characterizations of Nanomaterials. Figure 1A,B shows the scanning electron microscopy (SEM) images of $CuInS_2$ with different magnifications. As we can see, $CuInS_2$ exhibited a flower-like morphology, and the $CuInS_2$ microflowers (MFs) showed diameters ranging from 2.5 to 3.5 μm. The surfaces of $CuInS_2$ MFs are composed of $CuInS_2$ nanosheets, which has a thickness of about 30 nm. Figure 1C shows the scanning electron microscopy−energy-dispersive spectroscopy (SEM-EDS) mapping of the $CuInS_2$ MFs, which showed a very uniform distribution of Cu, In, and S elements in $CuInS_2$ MFs. Figure 1D,E depicts the transmission electron microscopy (TEM) images of OA-capped $NaYF_4$:Yb,Er (OA-UCNPs). As we can see from Figure 1D, OA-UCNPs showed a uniform hexagonal plate-like morphology. Figure 1E indicates that the UCNPs have mean sizes of approximately 150 nm. The scanning transmission electron microscopy (STEM) images and EDS mapping of $NaYF_4$:Yb,Er are shown in Figure 1F, which depicted the uniformly distributed elements within $NaYF_4$:Yb,Er, including Na, Y, F, Yb, and Er, confirming the successful synthesis of UCNPs. Moreover, the X-ray diffraction (XRD) analyses of $CuInS_2$ MFs and $NaYF_4$:Yb,Er (UCNPs) were also studied, and the detailed results (Figure S1, Supporting Information) indicated the successful synthesis of flower-like $CuInS_2$ and crystal hexagonal plate-like OA-UCNPs.

In addition, the successful synthesis of PAA-coated UCNPs was verified by Fourier transform infrared (FT-IR) spectroscopy, and the details are shown in Figure S2A. In addition, the upconversion fluorescence (FL) spectra of PAA@UCNPs and Ce6-Ab_2-PAA@UCNPs bioconjugates and the photocurrent responses of the proposed sensing platform toward the detection of 4 ng/mL PSA with Ab_2-PAA@UCNPs and Ce6-Ab_2-PAA@UCNPs as the signal labels were also investigated. As depicted in Figure S2B, compared with PAA-functionalized UCNPs, the FL intensity of Ce6-Ab_2-PAA@UCNPs bioconjugates only showed a slight drop, indicating that the modification only has minimal effects on the FL intensity, which was beneficial for the naked-eye readout. Figure S2C shows the photocurrent responses of Ab_2-PAA@UCNPs (black curve) and Ce6-Ab_2-PAA@UCNPs (red curve) as the signal labels. The modification of Ce6 to the Ab_2-PAA@UCNPs bioconjugates further enhanced the photocurrent restrain effect of Ab_2-PAA@UCNPs, which means that the sensitivity of the PEC sensing was improved.

Figure S3 shows the TEM images of PAA@UCNPs and Ab_2-PAA@UCNPs bioconjugates. The inset in Figure S3A depicts that the polymer layer on UCNPs is about 1 nm thick. After the formation of Ab_2-PAA@UCNPs bioconjugates (Figure S3B), the diameter of PAA@UCNPs increased, and a gray membrane was observed, which visually proved the successful modification of Ab_2 to PAA@UCNPs. In addition, UV−vis absorption spectroscopy was used to further demonstrate the formation of Ab_2-PAA@UCNPs and Ce6-Ab_2-PAA@UCNPs bioconjugates. Figure S3C depicts the absorption spectra of PAA@UCNPs, Ab_2-PAA@UCNPs, Ce6, and Ce6-Ab_2-PAA@UCNPs. After Ab_2 combined with UCNPs, an absorption peak located at ∼280 nm was observed, indicating the successful formation of Ab_2-PAA@UCNPs bioconjugates. The Ce6-Ab_2-PAA@UCNPs bioconjugates and pure Ce6 showed a similar absorption spectrum, indicating that Ce6 was modified on the surface of Ab_2-PAA@UCNPs, and its chromophor had no variation after the conjugation.

Possible Mechanisms of the Proposed Sensing Platform. The possible work mechanisms of the proposed sensing platform are shown in Scheme 2. In this protocol, the $CuInS_2$ MFs were fixed onto the ITO glass and worked as an efficient NIR light collector and energy converter, which can achieve photoelectric conversion. Considering that $CuInS_2$ is a p-type semiconductor, the dissolved O_2 in the electrolyte played as the main electron acceptor for $CuInS_2$ MFs. Under 980 nm NIR irradiation, Ce6-Ab_2-PAA@UCNPs were used as

https://dx.doi.org/10.1021/acs.analchem.0c04802
Anal. Chem. 2021, 93, 3486−3492

Scheme 2. Schematic Illustration of the Mechanism for the Integrated NIR Fluorescence-Induced Naked-Eye Readout and Photoelectrochemical Sensing

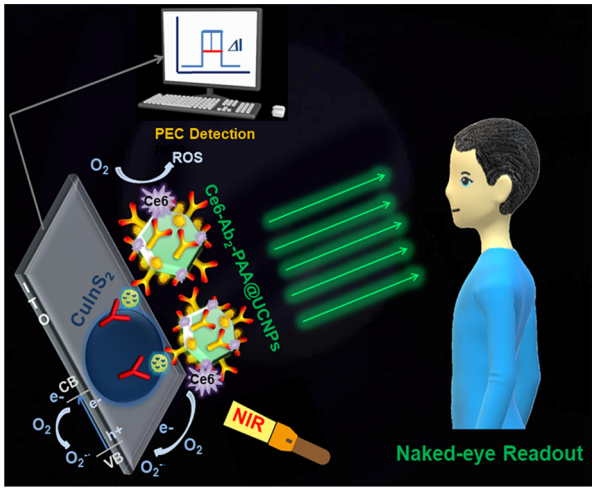

the signal generation center for both photocurrent suppression and green light fluorescence emission. For the PEC sensing function, on the one hand, Ce6-Ab_2-PAA@UCNPs worked as a poor conductor to reduce photocurrents; on the other hand, the addition of Ce6 could also consume the dissolved O_2 in the electrolyte,[31,32] while for the naked-eye NIR-FV readout, Ce6-Ab_2-PAA@UCNPs also could perform as an ideal illuminant body to produce visible green light. Moreover, the introduction of Ce6 to Ab_2-PAA@UCNPs would further reduce the output photocurrents and improve the sensitivity of the PEC function. By combining the $CuInS_2$ MF matrix and the Ce6-Ab_2-PAA@UCNPs bioconjugate label together and with the presence of the target analyte, we successfully constructed a dual-readout sensing platform.

Characterization of the Construction Process and Optimization of Experimental Conditions for the Sensing Platform. The photocurrents of each modified step during the building process were investigated, as shown in Figure 2A. After the modification of $CuInS_2$ to the ITO glasses, the photocurrent (curve b) reached the maximum level. Following this, after the modification of CHI (curve c), Ab_1 (curve d), BSA (curve e), PSA (curve f), and Ce6-Ab_2-PAA@UCNPs (curve g), the photocurrent response gets smaller gradually. The step-by-step decrease of photocurrents indicated the successful modification of each step. Electrochemical impedance spectroscopy (EIS) was used to characterize the interfacial properties of each construction step of the sensing platform. As shown in Figure 2B, the inset is the equivalent circuit containing R_s (the solution resistance), R_{et} (the electron transfer resistance), Z_w (the Warburg impedance), and C_{dl} (the double-layer capacitance). In the EIS Nyquist plots, R_{et} (the semicircle portion) was the most important index. The ITO showed a relatively small R_{et} (curve a); after the modification of $CuInS_2$ MFs, CHI, Ab_1, BSA, PSA, and Ce6-Ab_2-PAA@UCNPs, the semicircle part increased gradually, which proved the successful decoration of each poor-conductivity material. In addition, the simulated EIS data (via ZsimpWin) are provided in Table S1 (Supporting Information).

To obtain optimal sensing performance, some experimental conditions were optimized. As shown in Figure 2C, the photocurrent responses of different concentrations of $CuInS_2$-

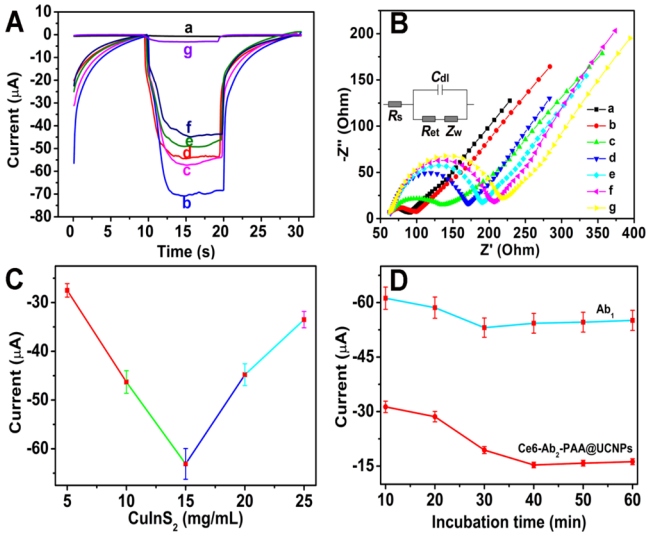

Figure 2. (A) Photocurrent responses and (B) EIS Nyquist plots of each modified electrode (a → g): (a) bare ITO; (b) ITO/$CuInS_2$; (c) ITO/$CuInS_2$/CHI; (d) ITO/$CuInS_2$/CHI/Ab_1; (e) ITO/$CuInS_2$/CHI/Ab_1/BSA; (f) ITO/$CuInS_2$/CHI/Ab_1/BSA/PSA; (g) ITO/$CuInS_2$/CHI/Ab_1/BSA/PSA/Ce6-Ab_2-PAA@UCNPs. (C) Effects of $CuInS_2$ concentration on the photocurrent response of the ITO/$CuInS_2$ electrode. (D) Incubation time for the CHI/Ab_1 and PSA/Ce6-Ab_2-PAA@UCNPs reaction on the photocurrent of the PEC immunoassay (note that the error bars show the standard deviation of three repeated measurements. Room temperature, PSA concentration was 4 ng/mL, and an applied power of 980 nm NIR was 10 W).

modified ITO electrodes were tested. With the concentrations of $CuInS_2$ solution increased from 5 to 15 mg/mL, the photocurrent reached the highest level; after that, the photocurrent began to fall, which indicated that 15 mg/mL is the best concentration for the PEC photocathode matrix. The reason may be because the concentrations of $CuInS_2$ solution lower or higher than 15 mg/mL could cause poor utilization of NIR or high impedance. Figure 2D depicts the optimization of the incubation time of Ab_1 (curve a) and PSA-Ce6-Ab_2-PAA@UCNPs (curve b) on the working electrode at room temperature. As we can see, with the increase of the incubation time of Ab_1 (reaction with CHI) and Ce6-Ab_2-PAA@UCNPs (reaction with PSA), the photocurrents decreased gradually (Ab_1: 10−30 min; Ce6-Ab_2-PAA@UCNPs: 10−40 min), and after that, the photocurrent response tended to level off, which means that a longer incubation time does not have a significant impact on the photocurrent signal. Hence, for time saving and efficiency, 30 and 40 min were selected as the optimal time for the Ab_1 and PSA-Ce6-Ab_2-PAA@UCNPs incubation.

Characteristics of the Analytical Performance of the Proposed Sensing Platform. Stability and reproducibility of a sensing platform are very important. To evaluate the practicability of the PEC sensing mode, the stability and reproducibility of the PEC mode were explored. For the stability testing of the fabricated sensing platform, the time-based photocurrent response of the ITO/$CuInS_2$ electrode was measured at "on−off−on" mode for 180 s, as depicted in Figure 3A; no noticeable photocurrent change was observed, indicating the good current output stability of the PEC mode sensing. Reproducibility of a sensing system is very important; herein, we used the intra-assay and the inter-assay that assessed the proposed sensing platform. The relative standard deviation

https://dx.doi.org/10.1021/acs.analchem.0c04802
Anal. Chem. 2021, 93, 3486−3492

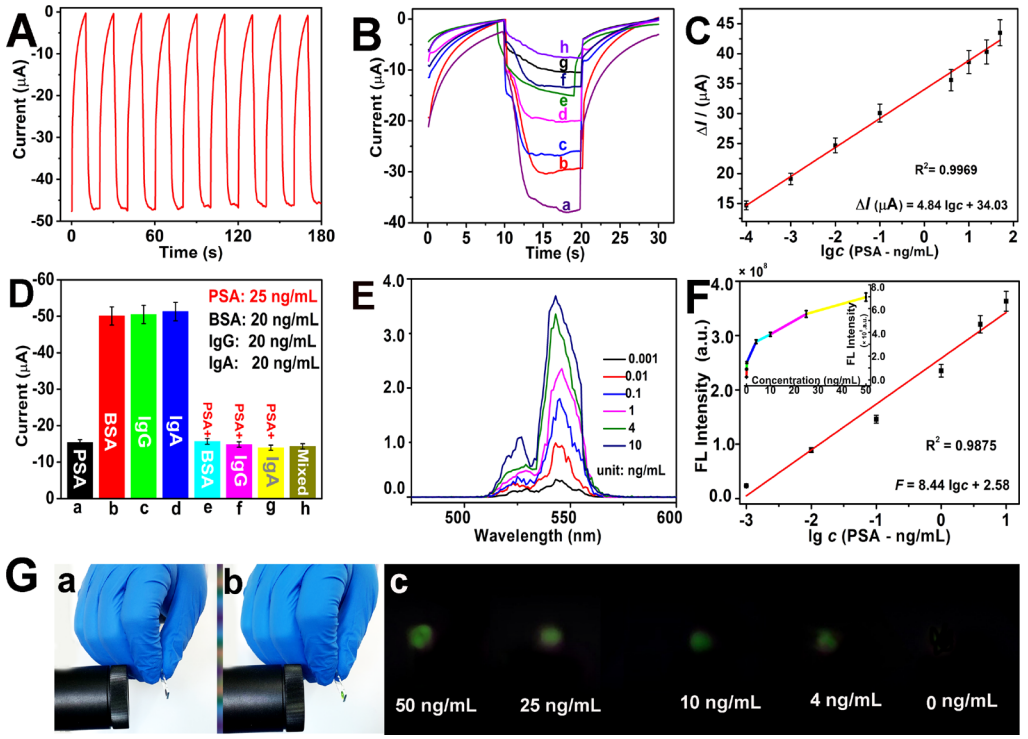

Figure 3. (A) Photocurrent responses of the $CuInS_2$/ITO electrode under repeated "off−on" irradiation cycles for 180 s. (B) Photocurrent response to different concentrations of PSA (a → h: 0.0001 ng/mL, 0.001 pg/mL, 0.01 ng/mL, 0.1 ng/mL, 4 ng/mL, 10 ng/mL, 25 ng/mL, and 50 ng/mL). (C) Calibration curve of the proposed PEC biosensor for the detection of different concentrations of PSA in the range of 0.0001−50 ng/mL. The error bars show the standard deviation of three repeated measurements. (D) Selectivity of the proposed PEC sensing platform: (a) PSA, (b) BSA, (c) IgG, (d) IgA, (e) PSA + BSA, (f) PSA + IgG, (g) PSA + IgA, and (h) PSA + BSA + IgG + IgA. (E) Upconversion FL spectra of the biosensor with varying concentrations of PSA (0.001, 0.01, 0.1, 1, 4, and 10 ng/mL). (F) Linear relationship between the FL intensity and the logarithm concentrations of PSA in the range of 0.001−10 ng/mL. The inset depicts the relativity between the concentrations of PSA and its FL intensities in the range of 0.001−50 ng/mL. The error bars indicate the standard deviation of three independent measurements. (G) Digital photographs of the fabricated biosensor with the 980 nm NIR laser (a) turned off and (b) on, which showed the color changing from black to green, and (c) digital photograph of the biosensor with different concentrations of PSA.

(RSD) of the same PSA concentration-modified electrode of the intra-assay and inter-assay is within 10% (data was not shown), which demonstrated the high reliability of the proposed sensing system.

To gain insight into the PEC and NIR-FV dual mode sensing mechanism and assess the viability of the proposed sensing platform, the fluorescence responses and the photocurrent of the optical response to PSA were examined. By using ITO/$CuInS_2$ as the photocathode and Ce6-Ab_2-PAA@UCNP bioconjugates as the signal label, the photocurrent response of different concentrations of PSA under optimal conditions and with 980 nm NIR light excitation (power: 10 W) was determined. Figure 3B depicts that the photocurrent response of the ITO/$CuInS_2$/CHI/Ab_1/BSA/PSA/Ce6-Ab_2-PAA@UCNP electrode decreased with increasing concentration (a → h: 0.0001, 0.001, 0.01, 0.1, 4, 10, 25, and 50 ng/mL) of PSA, which can be ascribed to the high impedance of Ce6-Ab_2-PAA@UCNPs and the O_2 consumption effect of Ce6. Figure 3C depicts the PEC mode for PSA analysis, and the dynamic linear range was 0.0001−50 ng/mL. In Tris−HCL buffer (0.1 M, pH = 7.0) solution, the regression equation for PSA detection was lg ΔI (μA) = 4.84 lg c + 34.03 ($\Delta I = I - I_0$, where I_0 and I are the photocurrent responses of the ITO/$CuInS_2$/CHI/Ab_1/BSA electrode before and after reaction with different concentrations of PSA/Ce6-Ab_2-PAA@UCNPs, respectively), with an LOD of about 0.03 pg/mL (S/N = 3) and a correlation coefficient of R^2 = 0.9969. Figure 3D shows the selectivity of the PEC sensing mode; as we can see, with the appearance of PSA (a-25 ng/mL PSA, 25 ng/mL PSA mixed with e-20 ng/mL BSA, f-20 ng/mL IgG, g-20 ng/mL IgA, and all their mixtures (h)), the photocurrent response of the biosensor was about −15 μA (a-25 ng/mL PSA) in the absence of PSA (b-20 ng/mL BSA, c-20 ng/mL IgG, and d-20 ng/mL IgA) and the photocurrent responses were much higher (about −49.5 μA), which proved the high target selectivity and robustness of the proposed sensing platform. As depicted in Figure 3E, the obtained FL intensities increased gradually with the increment of the corresponding PSA concentrations in the range of 0.001−10 ng/mL. The inset of Figure 3F shows the relationship of FL intensities versus PSA in the concentration range of 0.001−50 ng/mL. As shown in Figure 3F, in the dynamic range of 0.001−10 ng/mL, a good linear relationship was obtained between the FL intensities and the decimal logarithm of PSA concentrations lg c (ng/mL); the corresponding regression equation was F = 8.44 lg c + 2.58 (R^2 = 0.9875; n = 3).

Considering that the PSA normal threshold in healthy human serum is usually ≤4 ng/mL, the concentration of PSA is ≥10 ng/mL, indicating the increased risk of prostate cancer. The dynamic linear range of the proposed dual mode sensing platform perfectly covers the normal and abnormal PSA level in human serum, indicating that the proposed sensing platform has great significance in auxiliary clinical diagnosis. Based on the performance of PEC sensing and the naked-eye readout,

https://dx.doi.org/10.1021/acs.analchem.0c04802
Anal. Chem. 2021, 93, 3486−3492

Table 1. Performance Evaluation of the PEC Sensing Mode Analysis for PSA-Spiked Human Serum by Using the PSA ELISA Kit as a Reference

sample no.	add PSA (ng/mL)	PSA ELISA kit (ng/mL)	recovery (%)	PEC found (n = 3; ng/mL)	RSD (n = 3; %)	average (ng/mL)	recovery (%)
0	1	1.05	105.0	0.81, 1.03, 0.88	11	0.907	90.7
1	2	2.07	103.5	2.18, 2.29, 2.11	9.1	2.08	109.5
2	4	4.21	105.3	4.25, 4.35, 4.21	7.2	4.27	106.8
3	8	7.78	97.3	8.73, 8.61, 8.52	10	8.62	107.8

the proposed dual-readout sensing platform was absolutely competent for the rapid and sensitive bioanalysis. In addition, even compared with many published literature studies (Supporting Information, Table S2), our work also shows its advantage in analysis. Figure 3G (a and b) shows the digital photographs of the biosensor's color changing from black to green. The naked-eye readout performance of the sensing platform was also examined. Under irradiation from a 980 nm NIR laser (power: 8 W), different amounts of PSA were modified on the electrode, and the FL intensities decreased with the drop of PSA concentrations (Figure 3G-c). Even at the threshold level of PSA (4 ng/mL), the NIR-FV response could be observed. In addition, with a different illuminant body (different emission light and excitation light) design, this platform could achieve simultaneous naked-eye readout of different analytes and signals.

Real Sample Analysis. To evaluate the practical application of the designed sensing platform in real sample analysis, we detected the PSA concentrations in real human serum samples. In addition, a PSA enzyme-linked immunosorbent assay (ELISA) kit was used as the reference method for comparison. As we can see from Table 1, the RSD was within 11%, demonstrating the good repeatability of the sensing platform, while the recovery ranging from 90.7 to 109.5% indicated that there were no big differences between these two methods for the analysis of PSA in real human serum samples. These obtained results demonstrated the high accuracy and precision of the proposed sensing platform. Moreover, the design idea of integrating PEC sensing and naked-eye readout together can be extended to the detection of other biomolecules.

CONCLUSIONS

In summary, we successfully developed a dual-readout sensing platform that could achieve both the PEC and NIR-FV dual-readout analysis toward biomolecules. $CuInS_2$ shows a perfect photoelectric conversion efficiency (NIR to photocurrent) and could provide a high background PEC signal. By using PSA as a concept target, Ce6-Ab_2-PAA@UCNPs as the fluorophore/insulator, and $CuInS_2$ MFs as the photoactive matrix, the constructed biosensor could realize quick instrument-free naked-eye readout as well as high sensitivity and rapid and low background noise PEC sensing. Integrating naked-eye readout with PEC sensing together could help us quickly determine whether there are target analytes or not, especially benefitting portable detections. Moreover, the PEC and NIR-FV could act as the reference method to each other to improve the veracity of analysis. With the further development of the PEC and NIR-FV technique, we believe that the proposed design idea would become a convenient, cost-effective, and promising strategy for the design of sensing platforms.

ASSOCIATED CONTENT

Supporting Information

The Supporting Information is available free of charge at https://pubs.acs.org/doi/10.1021/acs.analchem.0c04802.

Some experimental details and attached figures and tables providing additional data (XRD, FT-IR spectra, TEM images, simulation parameters, and comparison of different methods for PSA detection) (PDF)

AUTHOR INFORMATION

Corresponding Author

Jin Ouyang − *Key Laboratory of Theoretical and Computational Photochemistry, Ministry of Education, College of Chemistry, Beijing Normal University, Beijing 100875, China;* orcid.org/0000-0002-0286-0798; Phone: 86 010-58805373; Email: jinoyang@bnu.edu.cn

Authors

Qingzhi Han − *Key Laboratory of Theoretical and Computational Photochemistry, Ministry of Education, College of Chemistry, Beijing Normal University, Beijing 100875, China*

Xuan Zhao − *Key Laboratory of Theoretical and Computational Photochemistry, Ministry of Education, College of Chemistry, Beijing Normal University, Beijing 100875, China*

Na Na − *Key Laboratory of Theoretical and Computational Photochemistry, Ministry of Education, College of Chemistry, Beijing Normal University, Beijing 100875, China;* orcid.org/0000-0002-0474-8409

Complete contact information is available at: https://pubs.acs.org/10.1021/acs.analchem.0c04802

Notes

The authors declare no competing financial interest.

ACKNOWLEDGMENTS

J.O. gratefully acknowledges the financial support from the National Natural Science Foundation of China (21974010 and 21675014). N.N. thanks the NNSF of China (21874012 and 21675015).

REFERENCES

(1) Zhang, K.; Zhou, H.; Mei, Q.; Wang, S.; Guan, G.; Liu, R.; Zhang, J.; Zhang, Z. *J. Am. Chem. Soc.* **2011**, *133*, 8424−8427.

(2) Zhao, X.; Gao, Y.; Wang, J.; Zhan, Y.; Lu, X.; Xu, S.; Luo, X. *Chem. Commun.* **2020**, *56*, 13828−13831.

(3) Zhang, D.; Wang, L.; Yuan, X.; Gong, Y.; Liu, H.; Zhang, J.; Zhang, X.; Liu, Y.; Tan, W. *Angew. Chem., Int. Ed.* **2020**, *59*, 695−699.

(4) Gu, K.; Xu, Y.; Li, H.; Guo, Z.; Zhu, S.; Zhu, S.; Shi, P.; James, T. D.; Tian, H.; Zhu, W. H. *J. Am. Chem. Soc.* **2016**, *138*, 5334−5340.

(5) Qiu, Z.; Shu, J.; Tang, D. *Anal. Chem.* **2017**, *89*, 5152−5160.

(6) Zhao, W. W.; Xu, J. J.; Chen, H. Y. *Chem. Soc. Rev.* **2015**, *44*, 729−741.

(7) Chu, Y.; Deng, A. P.; Wang, W.; Zhu, J. J. *Anal. Chem.* **2019**, *91*, 3619−3627.
(8) Shu, J.; Tang, D. *Anal. Chem.* **2020**, *92*, 363−377.
(9) Chi, H.; Han, Q.; Chi, T.; Xing, B.; Ma, N.; Wu, D.; Wei, Q. *Biosens. Bioelectron.* **2019**, *132*, 1−7.
(10) Han, Q.; Wang, R.; Xing, B.; Zhang, T.; Khan, M. S.; Wu, D.; Wei, Q. *Biosens. Bioelectron.* **2018**, *99*, 493−499.
(11) Han, Q.; Wang, H.; Wu, D.; Wei, Q. *Biosens. Bioelectron.* **2021**, *173*, 112803.
(12) Xu, Y. T.; Yu, S. Y.; Zhu, Y. C.; Fan, G. C.; Han, D. M.; Qu, P.; Zhao, W. W. *TrAC Trends Anal. Chem.* **2019**, *114*, 81−88.
(13) Han, Q.; Chi, H.; Wang, H.; Wu, D.; Wei, Q. *Anal. Chim. Acta* **2019**, *1092*, 85−92.
(14) Han, Q.; Wang, H.; Qi, Y.; Wu, D.; Wei, Q. *Nanoscale Adv.* **2019**, *1*, 4313−4320.
(15) Fan, G. C.; Shi, X. M.; Zhang, J. R.; Zhu, J. J. *Anal. Chem.* **2016**, *88*, 10352−10356.
(16) Chen, W.; Qi, J.; Dong, C.; Chen, J.; Shen, Z.; He, Y.; Yang, S.; Chen, T.; Chen, C.; Li, Y.; Li, M. D.; Wang, M. *ACS Appl. Energy Mater.* **2019**, *2*, 5231−5242.
(17) Yu, C.; Zhang, L.; Tian, L.; Liu, D.; Chen, F.; Wang, C. *CrystEngComm* **2014**, *16*, 9596−9602.
(18) Xia, C.; Meeldijk, J. D.; Gerritsen, H. C.; de Mello Donega, C. *Chem. Mater.* **2017**, *29*, 4940−4951.
(19) Haase, M.; Schäfer, H. *Angew. Chem., Int. Ed.* **2011**, *50*, 5808−5829.
(20) Wilhelm, S. *ACS Nano* **2017**, *11*, 10644−10653.
(21) Zhou, B.; Shi, B.; Jin, D.; Liu, X. *Nat. Nanotechnol.* **2015**, *10*, 924−936.
(22) Liang, L.; Liu, Y.; Bu, C.; Guo, K.; Sun, W.; Huang, N.; Peng, T.; Sebo, B.; Pan, M.; Liu, W.; Guo, S.; Zhao, X. Z. *Adv. Mater.* **2013**, *25*, 2174−2180.
(23) Lv, S.; Zhang, K.; Zhu, L.; Tang, D. *Anal. Chem.* **2019**, *92*, 1470−1476.
(24) Qiu, Z.; Shu, J.; Tang, D. *Anal. Chem.* **2018**, *90*, 12214−12220.
(25) Luo, Z.; Zhang, L.; Zeng, R.; Su, L.; Tang, D. *Anal. Chem.* **2018**, *90*, 9568−9575.
(26) Qiu, Z.; Shu, J.; Tang, D. *Anal. Chem.* **2018**, *90*, 1021−1028.
(27) Li, Z.; Zhang, Y.; Jiang, S. *Adv. Mater.* **2008**, *20*, 4765−4769.
(28) Xu, J.; Xu, L.; Wang, C.; Yang, R.; Zhuang, Q.; Han, X.; Dong, Z.; Zhu, W.; Peng, R.; Liu, Z. *ACS Nano* **2017**, *11*, 4463−4474.
(29) Zhu, L.; Liu, J.; Zhou, G.; Ng, H. M.; Ang, I. L.; Ma, G.; Liu, Y.; Yang, S.; Zhang, F.; Miao, K.; Poon, T. C. W.; Zhang, X.; Yuan, Z.; Deng, C. X.; Zhao, Q. *Chem. Commun.* **2019**, *55*, 14255−14258.
(30) Jin, B.; Wang, S.; Lin, M.; Jin, Y.; Zhang, S.; Cui, X.; Gong, Y.; Li, A.; Xu, F.; Lu, T. J. *Biosens. Bioelectron.* **2017**, *90*, 525−533.
(31) Dong, Z.; Feng, L.; Hao, Y.; Chen, M.; Gao, M.; Chao, Y.; Zhao, H.; Zhu, W.; Liu, J.; Liang, C.; Zhang, Q.; Liu, Z. *J. Am. Chem. Soc.* **2018**, *140*, 2165−2178.
(32) Zhu, Z.; Tang, Z.; Phillips, J. A.; Yang, R.; Wang, H.; Tan, W. *J. Am. Chem. Soc.* **2008**, *130*, 10856−10857.

https://dx.doi.org/10.1021/acs.analchem.0c04802
Anal. Chem. 2021, 93, 3486−3492